Research on Engineering Structures & Materials
www.jresm.org
Research Group

*Research Article*

# Effect of abrasive water jet surface hardening on the fatigue life of aerospace-grade titanium alloys

Li Zhang [*,a]

*College of Intelligent Manufacturing and Information Engineering, Sichuan Technology and Business College, Chengdu, Sichuan, 611830, China*

**Article Info**

***Article History:***

Received 02 Jul 2026

Accepted 14 Sep 2026

***Keywords:***

Abrasive waterjet;
Aerospace titanium alloys;
Fatigue life prediction;
Residual stress;
Data fusion

**Abstract**

Abrasive water jet surface hardening can improve the fatigue resistance of aerospace-grade titanium alloys by modifying surface integrity and residual stress. A quantitative framework linking process parameters, surface characteristics, and fatigue life was established for Ti-6Al-4V alloy. Particle impact dynamics were combined with surface roughness, grain size, hardness, and residual stress measurements to construct a fatigue-life prediction model. Experiments were conducted under different jet pressures, abrasive particle sizes, and exposure times. The results show that the combination of 220 MPa jet pressure and 100-mesh abrasive produced a fatigue life of $2.05 \times 10^5$ cycles. Model prediction errors remained within 2.8%–4.8%. The results demonstrate that fatigue improvement depends on the coordinated effects of residual compressive stress, surface hardening, and roughness control, providing a quantitative basis for optimizing abrasive water jet strengthening parameters.

© 2026 MIM Research Group. All rights reserved.

## 1. Introduction

With the increasing demand for reliable surface engineering in advanced manufacturing, quantitative analysis of strengthening mechanisms and fatigue performance has become increasingly important. Titanium alloys are widely used in aerospace structures because of their high specific strength and corrosion resistance, while their fatigue performance remains highly sensitive to surface integrity. Titanium alloy with high specific strength and excellent corrosion resistance is commonly used in aerospace equipment, but its surface integrity has a great impact on fatigue life. The microdefects that exist in the surface layer can easily lead to fatigue crack initiation, especially under the synergistic effect of alternating loads and complex environments. By impact-induced high-speed particle jetting, abrasive waterjet strengthening is a powerful surface modification process that can leave compressive residual stress and a layer of plastic deformation in the surface of materials [1], which plays an important role in the fatigue life improvement of titanium alloy.

Yao et al. [1] demonstrated that micro-abrasive water jet peening can improve the residual stress distribution and fatigue performance of TA19 titanium alloy. Wan et al. [2] investigated the microstructural evolution and tension–tension fatigue behavior of Ti-6Al-4V and identified the combined effects of grain refinement and dislocation evolution. Song et al. [3] reported that deflecting abrasive water jet peening improved surface integrity, while Wan et al. [4] confirmed its effectiveness in suppressing fatigue crack propagation. Lv et al. [5] examined the effects of process parameters on roughness and residual stress, and Soori and Arezoo [6] considered their coordinated optimization. Recent studies have further extended abrasive water jet treatment to curved surfaces and alternative jet-assisted surface modification methods [7,8]. Earlier studies published during 2015–2019 should also be incorporated to establish the development of water-

*Corresponding author: zhannglii@outlook.com
[a]orcid.org/ 0009-0005-8729-2484
DOI: http://dx.doi.org/10.17515/resm2026-1813im0702rs

jet strengthening, surface-integrity evaluation, and fatigue modeling techniques over a broader research period.

Previous studies have separately investigated abrasive water jet process optimization, residual stress evolution, surface integrity, and fatigue behavior. However, the quantitative relationship among process parameters, near-surface characteristics, and fatigue performance remains insufficiently integrated, particularly under multi-parameter coupling conditions. The specific contribution lies in establishing a unified process–surface integrity–fatigue framework that links jet pressure, abrasive mesh size, exposure time, surface roughness, residual stress, and fatigue life. Impact mechanics and multi-source experimental data are combined to characterize the strengthening response and construct a fatigue-life prediction model. The framework is evaluated under different processing conditions to identify the balance between beneficial residual compressive stress and detrimental roughness-induced stress concentration. This approach provides a quantitative basis for interpreting the strengthening mechanism and for optimizing abrasive water jet surface treatment within the investigated parameter range.

## 2. Modeling and Material Property Analysis of Strengthened Titanium Alloys

### 2.1 Mechanical Properties of Aerospace-Grade Titanium Alloys

Aerospace-grade titanium alloys exhibit high specific strength, good fracture toughness, and excellent corrosion resistance, while their surface deformation and fatigue response are closely related to their mechanical properties. Ti-6Al-4V was selected as the representative aerospace material. Its tensile strength is approximately 895–980 MPa, yield strength is 825–900 MPa, elastic modulus is about 110 GPa, and Poisson's ratio ranges from 0.31 to 0.34. The alloy also exhibits a microhardness of approximately 320 HV and a fatigue strength of about 500–600 MPa. These properties provide high load-bearing capacity while allowing localized plastic deformation under high-speed abrasive particle impact. Previous investigations of axial jet systems have further shown that mixing-chamber configuration, inlet swirling flow, and water–oil operating conditions affect jet momentum transfer, pressure characteristics, and the mechanical response of engineering components [38,39]. These findings provide complementary engineering evidence for evaluating material behavior under jet-induced loading and support the subsequent analysis of plastic deformation, residual stress evolution, and fatigue enhancement in Ti-6Al-4V.

### 2.2 Modeling the Influence of Surface Integrity on Fatigue Failure Mechanisms

After abrasive water jet strengthening, fatigue life is jointly affected by surface roughness, residual compressive stress, and surface hardening. Increased compressive stress and hardness can delay crack initiation, whereas excessive roughness promotes local stress concentration. Based on the surface-integrity and fatigue-damage relationships reported in Ref. [9], fatigue life is expressed as a composite function of these parameters:

$$N_f = K \cdot \sigma_a^{-m} \cdot \left(1+\frac{|\sigma_r|}{\sigma_y}\right)^{\alpha} \cdot \left(1+\frac{H_s - H_0}{H_0}\right)^{\beta} \cdot \left(1+R_a\right)^{-\gamma} \tag{1}$$

where $N_f$ is the fatigue life; $K$ is a material constant; $\sigma_a$ is the cyclic stress amplitude; $m$ is the fatigue sensitivity index; $\sigma_r$ is the surface residual compressive stress; $\sigma_y$ is the material yield strength; $H_s$ is the hardened surface layer hardness; $H_0$ is the original hardness; $R_a$ is the surface roughness; and $\alpha$、$\beta$、$\gamma$ are the weighting coefficients for each influencing factor.

Fatigue damage evolution is further described using the surface-defect-driven formulation reported in Ref. [9]:

$$D = \frac{n}{N} = \frac{1}{C}\left(\frac{\sigma_{\max}\left(1+\eta R_a\right) - \sigma_r}{H_s}\right)^{b} \tag{2}$$

where $D$ represents the fatigue damage variable, $n$ is the actual number of cycles, and the remaining coefficients describe cyclic stress, roughness, and material-dependent effects. The formulation indicates that residual compressive stress and surface hardening suppress fatigue-damage accumulation, whereas increasing roughness accelerates crack initiation.

Experimental and computational studies of jet-driven systems have shown that coupled modeling is effective for evaluating the nonlinear effects of geometric configuration, surface roughness, and operating parameters on flow and performance characteristics. The influence of motive nozzle spacing and surface roughness has been investigated through combined experimental and computational approaches [40], while the effect of motive nozzle exit length has also been quantified using numerical simulation supported by experimental validation [41]. Similar computational–experimental methods have been applied to water-jet pump performance analysis, demonstrating the reliability of integrated modeling for describing complex jet-induced interactions [42]. These approaches provide useful methodological support for establishing the relationship among abrasive waterjet process parameters, surface integrity evolution, and fatigue failure behavior.

### 2.3 Surface Strengthening Requirements and Problem Formulation

Titanium alloy components in the aerospace service environment endure long-term high-frequency alternating loads and complex stress superposition. It is well known that fatigue cracks originate from microdefects or stress concentration areas on the surface. Thus, the dimensional goal of surface strengthening mainly focuses on crack initiation inhibition and delaying propagation through the integration of residual compressive stress, varied surface hardness and optimized surface topography. Surface strengthening can therefore be formulated as a multi-parameter optimization problem that maximizes fatigue resistance while maintaining acceptable surface quality. Based on the surface-strengthening and fatigue-performance relationship summarized in Ref. [10], residual stress, hardness variation, and surface roughness are incorporated into the fatigue-strength expression:

$$\sigma_f' = \sigma_0 + \lambda \cdot \left|\sigma_r\right| + \mu \cdot \left(H_s - H_0\right) - \upsilon \cdot R_a \tag{3}$$

where $\sigma_f'$ is the fatigue strength after strengthening; $\sigma_0$ is the initial fatigue strength of the material; $\sigma_r$ is the residual compressive stress; $H_s$ and $H_0$ are the post-strengthening and initial hardness, respectively; $R_a$ is the surface roughness; and $\lambda$、$\mu$、$\upsilon$ is the influence weight coefficient.

The problem of improving fatigue life is formulated as a constrained optimization problem:

$$\max N_f = f\left(P, d, t\right) \quad \text{s.t.} \quad R_a \le R_{\lim}, \sigma_r \ge \sigma_{\min} \tag{4}$$

where $N_f$ represents fatigue life; $P$ represents jet pressure; $d$ represents abrasive particle size; $t$ represents exposure time; $R_{\lim}$ represents the maximum allowable roughness; and $\sigma_{\min}$ represents the required minimum residual compressive stress [11]. This model demonstrates that surface strengthening is essentially a process of achieving optimal performance matching under the constraints of multiple process parameters, providing a clear theoretical description for subsequent strengthening parameter design and experimental optimization.

## 3. Modeling Abrasive Waterjet Surface Strengthening Processes and Parameters

In this novel process, the surface of a material is subjected to high-speed impacts by abrasive particles propelled by a high-velocity water jet at frequencies on the order of kilohertz, which leads to plastic deformation and enhanced residual compressive stress in the surface layer. The basic strengthening mechanism is illustrated in Figure 1. Under a prescribed jet pressure, abrasive particles acquire high impact velocity and induce localized plastic deformation and residual

compressive stress in the near-surface region. The schematic representation is established according to the abrasive water jet impact mechanism reported in the related literature [12].

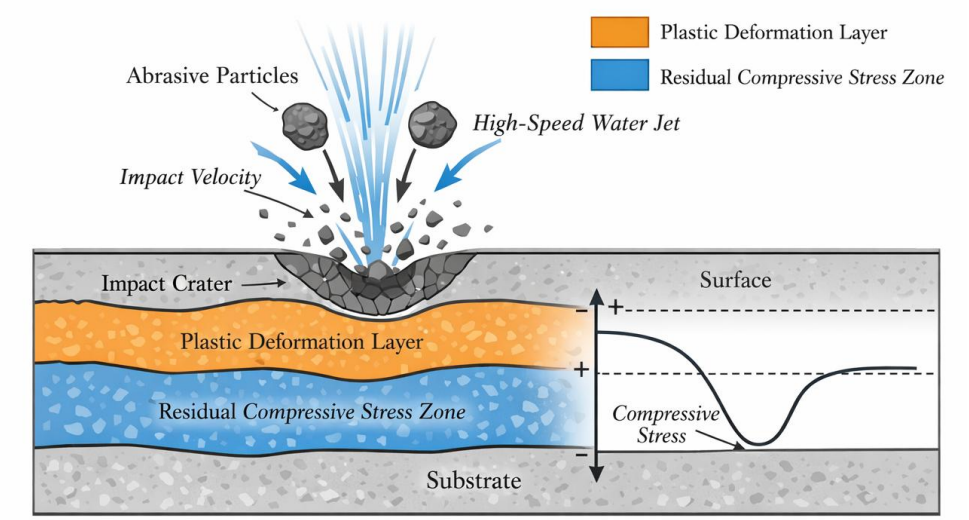



Fig. 1. Schematic diagram of the abrasive water jet surface strengthening process

The impact velocity $\upsilon$ can be approximately expressed by the energy conservation equation as:

$$\upsilon = C_{\upsilon}\sqrt{\frac{2P}{\rho}} \tag{5}$$

where $\upsilon$ is the particle impact velocity; $C_{\upsilon}$ is the velocity coefficient; $P$ is the injection pressure; and $\rho$ is the fluid density. This relationship indicates that injection pressure is the key parameter determining impact intensity [12].

Under the coupled action of multiple parameters, the strengthening effect depends not only on pressure but is also closely related to abrasive particle size $d$, jet distance $S$, and exposure time $t$ [13]. To describe the mapping relationship between process parameters and surface properties, a unified functional model can be constructed, as shown in Figure 2:

$$\sigma_r = f\left(P, d, S, t\right) \tag{6}$$

where $\sigma_r$ represents the residual compressive stress on the surface [14]. Incorporating fatigue life into the unified analytical framework, it can be expressed as:

$$N_f = g\left(\sigma_r, H_s, R_a\right) \tag{7}$$

In the equation, $N_f$ represents fatigue life; $H_s$ represents surface hardness; and $R_a$ represents surface roughness [15]. The above model illustrates the hierarchical relationship between "process parameters—surface integrity—fatigue performance."

To characterize the stress distribution during the impact process, impact dynamics simulation analysis was introduced, as shown in Figure 3. Based on elastoplastic contact theory, the maximum contact stress induced by particle impact can be approximately expressed as:

$$\sigma_{\max} = k\left(\frac{m\upsilon^2}{d^3}\right)^{\frac{1}{2}} \tag{8}$$

where $\sigma_{\max}$ is the maximum contact stress; $k$ is the material-dependent coefficient; $m$ is the particle mass; $\upsilon$ is the impact velocity; and $d$ is the contact characteristic dimension [16].

Simulation results indicate that the stress field exhibits a gradient decay distribution with depth, with a significant compressive stress concentration zone forming in the surface layer.

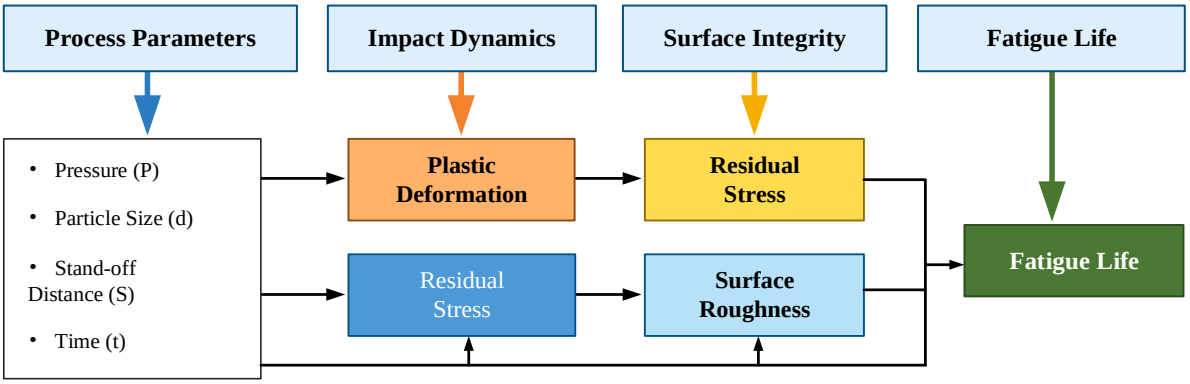



Fig. 2. Process parameter–performance mapping framework

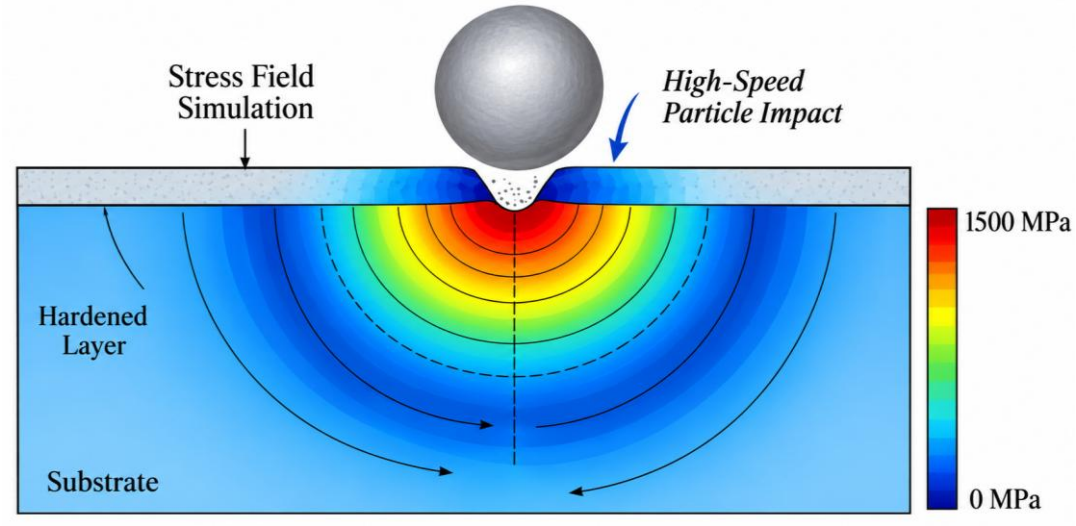



Fig. 3. Schematic representation of the impact-induced stress field

The qualitative stress distribution induced by high-speed particle impact is illustrated schematically in Figure 3. The stress concentration is strongest near the impact region and gradually decreases with increasing distance from the contact zone.

Overall, the strengthening process of abrasive waterjet is essentially a nonlinear dynamic process driven by the coupling of multiple parameters. The construction of a process parameter-surface property mapping model combined with impact dynamics simulation analysis can provide theoretical support for optimizing the strengthening process and improving fatigue life[17].

## 4. Surface Characterization and Multi-Source Data Acquisition

### 4.1 Surface Topography and Roughness Analysis

After abrasive waterjet strengthening, the surface morphology of the material is dramatically changed and may appear in the form of regularly spaced micro-pits and evidence of plastic movement, with the common features depicted in Figure 4. The reinforced surface layer, in comparison to the untreated surface, has clear impact marks and localized densification; it is a microstructure that creates stress concentration dispersal and prevents crack formation [18]. To quantitatively characterize surface roughness, the arithmetic mean roughness parameter $R_a$ is introduced:

$$R_a = \frac{1}{L}\int_0^L \left| z(x) \right| dx \tag{9}$$

where $R_a$ is the surface roughness; $L$ is the sampling length; and $z(x)$ is the surface profile height function [19].

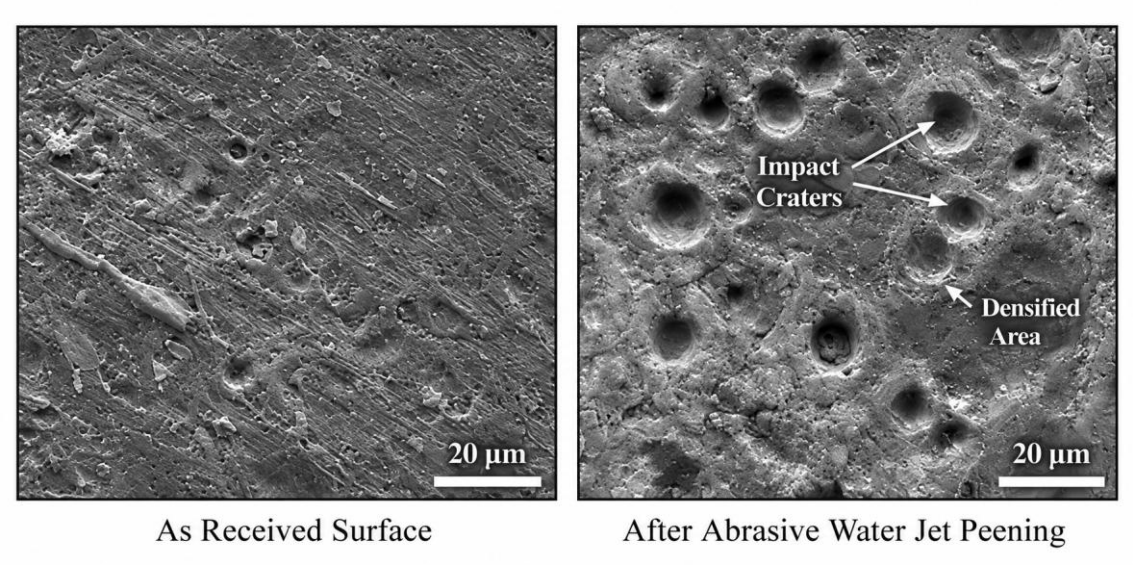



Fig. 4. SEM comparison of surface topography

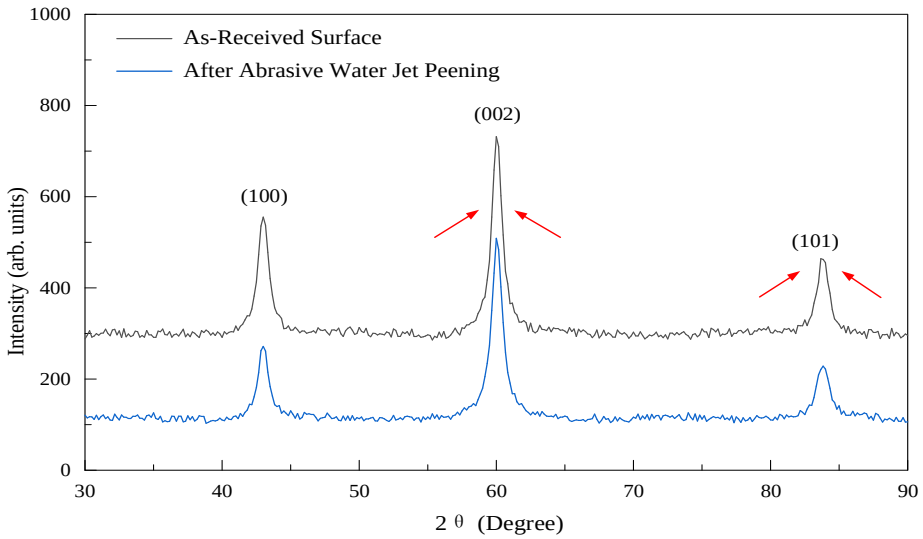



Fig. 5. Comparison of XRD diffraction patterns

Surface roughness has a significant impact on fatigue performance, and its effect can be expressed by the stress concentration factor:

$$K_t = 1 + \beta \cdot \frac{R_a}{r} \tag{10}$$

where $K_t$ is the stress concentration factor; $\beta$ is an empirical coefficient; and $r$ is the characteristic radius of curvature of the surface [20]. It can be seen that moderate surface roughening is conducive to the formation of a compressive stress layer, while excessive roughness will exacerbate stress concentration, which is detrimental to improving fatigue performance.

### 4.2 Crystal Structure and XRD Characterization

During abrasive waterjet strengthening, the surface crystal structure is distorted and refined by means of the high-speed impact, which is characterized by the reduction of the grain size and the increase of the number of dislocations. The characteristics of structural evolution are depicted in Figure 5. XRD patterns exhibit measurable peak broadening and slight peak shifts after abrasive

water jet treatment. These variations indicate changes in lattice strain and crystallographic response. Because peak broadening may result from both finite crystallite size and microstrain, grain refinement is treated as a possible contributing mechanism rather than being determined solely from peak width [21]. Grain size can be estimated using the Scherrer formula:

$$D = \frac{K\lambda}{\theta \cos\theta} \tag{11}$$

where $D$ is the grain size; $k$ is the shape factor; $\lambda$ is the X-ray wavelength; β\betaβ is the half-width at half-maximum of the diffraction peak; and $\theta$ is the Bragg angle [22].

Minor shifts in diffraction peak positions can be used to calculate lattice strain:

$$\varepsilon = \frac{\Delta d}{d_0} \tag{12}$$

where $\varepsilon$ is the lattice strain; $d_0$ is the original interplanar spacing; and $\Delta d$ is the change [23].

### 4.3 Residual Stress Testing and Distribution Characteristics

After abrasive waterjet strengthening, a significant compressive residual stress layer forms on the material's surface, and its distribution characteristics have a decisive influence on fatigue performance. X-ray diffraction was used to test residual stresses, with the stress state determined by measuring changes in crystal plane spacing [24]. Based on the $\sin^2\psi$ method, residual stress can be expressed as:

$$\sigma_r = \frac{E}{1+\nu} \cdot \frac{\Delta d}{d_0} \tag{13}$$

where $\sigma_r$ is the residual stress; $E$ is the elastic modulus; $\nu$ is the Poisson's ratio; $d_0$ is the interplanar spacing in the stress-free state; and $\Delta d$ is the change in interplanar spacing after loading [25].

Along the depth direction, residual stress decreases gradually from the near-surface region toward the substrate. Experimental results further show that the measured surface residual compressive stress varied from approximately −320 MPa to −512 MPa under different strengthening conditions. This variation confirms the strong dependence of the residual stress field on jet pressure and exposure time; this trend can be described by an exponential function:

$$\sigma(z) =_0 \exp(-kz) \tag{14}$$

where $\sigma(z)$ is the residual stress at depth $z$; $\sigma_0$ is the surface residual stress; and $k$ is the decay coefficient [26].

### 4.4 Fusion of Multi-Source Experimental Data and Feature Construction

In order to describe the impact of abrasive waterjet strengthening on the material properties in a comprehensive way, one will have to combine the results of the experiments in a variety of sources such as the surface topography, crystal structure, and residual stress. Multi-source data has high dimensionality, non-consistent units and complicated correlations and information integration is achieved by building coherent features [27]. The result of various sources is normalized to remove the difference in dimensions and the expression is:

$$x_i' = \frac{x_i - x_{\min}}{x_{\max} - x_{\min}} \tag{15}$$

where $x_i$ represents the raw data; $x_i'$ represents the normalized result; $x_{\min}$ and $x_{\max}$ denote the minimum and maximum values of the feature, respectively [28].

Constructing the comprehensive surface integrity feature vector:

$$\mathrm{F}=\left[R_a, D, \varepsilon, \sigma_r, H_s\right] \tag{16}$$

where $\mathrm{F}$ is the feature vector; $R_a$ is the surface roughness; $D$ is the grain size; $\varepsilon$ is the lattice strain; $\sigma_r$ is the residual stress; and $H_s$ is the surface hardness [29].

To enhance the expressive power of the features, a weighted fusion model can be introduced:

$$F_{\text{fusion}}=\sum_{i=1}^{n} w_i x_i' \tag{17}$$

In the equation, $F_{\text{fusion}}$ represents the fused eigenvalue; $w_i$ denotes the weight coefficients for each eigenvalue, satisfying $\sum w_i=1$. By adjusting these weights, key influencing factors can be highlighted, thereby providing high-quality input for subsequent fatigue life prediction models and improving the accuracy and stability of the analysis [30].

## 5. Strengthening Mechanism and Residual Stress Field Evolution Model

### 5.1 Kinetic Analysis of Surface Plastic Deformation

During abrasive waterjet strengthening, the intense impacts of particles cause the material to undergo severe plastic deformation on the surface and its development is jointly regulated by the impact kinetic energy and material constitutive properties as well as strain rate [31]. During the impact, the conditions of high strain rate loading in the contact zone are created, which leads to the immediate transition of the local area to a yield state and a plastic flow; its spatial distribution characteristic is illustrated in Figure 6.

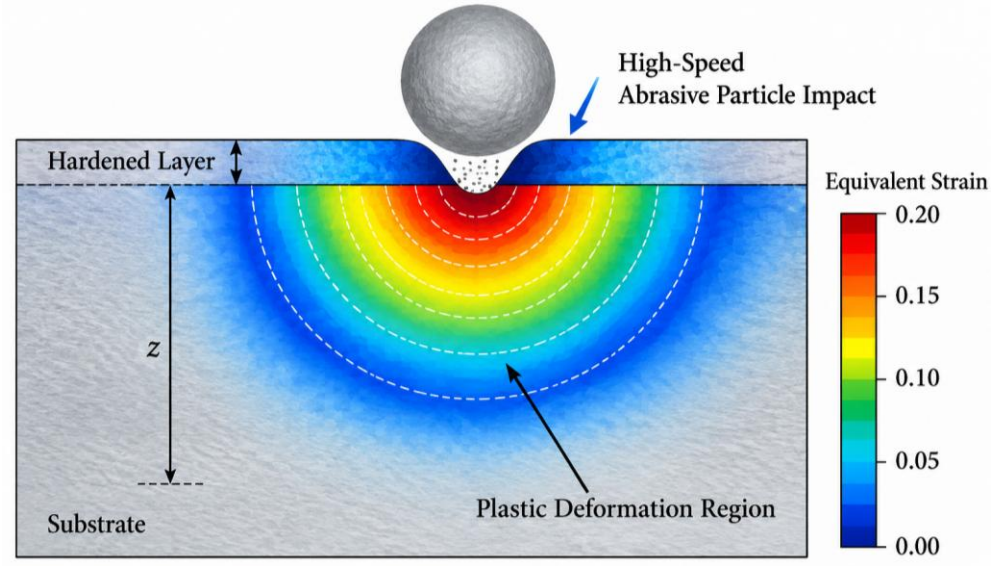



Fig. 6. Schematic representation of the plastic deformation region and equivalent strain distribution

Based on the relationship between momentum and energy conversion, the equivalent strain caused by particle impact can be expressed as:

$$\varepsilon_{\text{ep}}=C_1\left(\frac{\rho \upsilon^2}{\sigma_y}\right)^n \tag{18}$$

where $\varepsilon_{\text{ep}}$ is the equivalent plastic strain; $C_1$ is an empirical coefficient; $\rho$ is the material density; $\upsilon$ is the impact velocity; $\sigma_y$ is the yield strength; and $n$ is the material's strain sensitivity index, with the ratio of impact velocity to material strength determining the extent of plastic deformation [32].

Further considering the decay law of the strain field along the depth direction, it can be described using an exponential function:

$$\varepsilon(z) = \varepsilon_0 \exp(-\alpha z) \tag{19}$$

where $\varepsilon(z)$ is the equivalent strain at depth $z$; $\varepsilon_0$ is the maximum surface strain; and $\alpha$ is the attenuation coefficient [33]. As shown in Figure 6, the strain field reaches a peak in the central impact region and gradually diffuses and attenuates radially and with depth, forming a typical "hemispherical" plastic deformation zone.

Figure 6 schematically illustrates the expected spatial distribution of plastic deformation beneath the particle impact region. The contour pattern is used to represent the qualitative decay of deformation with depth and radial distance and should not be interpreted as independently validated finite-element data.

### 5.2 Residual Stress Field Distribution Model

Following abrasive waterjet strengthening, a non-uniform residual stress field is developed in the surface layer of the material due to the combined influences of high-speed impact and plastic flow. Residual compressive stress dominates the surface and near-surface regions in this field and gradually lessens as the depth increases and changes to a stable state as one moves towards the matrix [34]. The stress field formation is directly proportional to the impact energy of the particles, the level of plastic deformation and the elastic-plastic recovery ability of the material.

The depth-dependent residual-stress distribution follows the exponential approximation defined previously in Equation (14). Section 5.2 therefore focuses on the physical interpretation of stress-field evolution rather than introducing a duplicate mathematical expression:

$$\sigma_r(z) = \sigma_s \exp(-kz) \tag{20}$$

where $\sigma_r(z)$ is the residual stress at depth $z$; $\sigma_s$ is the peak surface residual stress; and $k$ is the stress decay coefficient. This model indicates that the strengthening effect is primarily concentrated in the near-surface region; as the impact energy is transferred inward and gradually dissipated, the amplitude of the residual compressive stress continuously decreases [35].

To account for the influence of the transverse position on the stress field distribution, a two-dimensional Gaussian approximation model can be further established:

$$\sigma_r(x,z) = \sigma_0 \exp\left[-\left(\frac{x^2}{a^2} + \frac{z^2}{b^2}\right)\right] \tag{21}$$

where $\sigma_r(x,z)$ represents the residual stress resulting from the combined effects of the lateral position $x$ and the depth $z$; $\sigma_0$ denotes the maximum residual compressive stress at the impact center; and $a$ and $b$ are the lateral and longitudinal influence scale parameters, respectively [36]. This equation captures the spatial distribution characteristics of the residual stress field, which is maximum at the impact center and gradually diffuses and decays toward the surrounding regions.

### 5.3 Coupling of Microstructural Evolution and Strengthening Mechanisms

During the process of abrasive waterjet strengthening, the surface structure of the material experiences a strong microstructural evolution under the continuous action of high-speed particles, which creates a combined effect with plastic deformation strengthening, residual stress strengthening, and grain refinement strengthening. Based on previously reported abrasive water jet strengthening mechanisms, repeated high-speed particle impact may promote dislocation accumulation, local lattice distortion, and microstructural refinement in the near-surface region. These mechanisms can contribute to surface hardening and stabilization of residual compressive stress. Because direct quantitative dislocation and grain-orientation measurements were not

included in the present experimental programmed, these microstructural processes are interpreted as literature-supported mechanisms rather than independently verified observations [37].

The strengthening mechanism involves not only microstructural evolution but also the redistribution of the stress field. On the one hand, dislocation proliferation and lattice distortion increase the stored energy in the surface layer and improve the capacity of the material to delay crack formation; on the other hand, grain refinement makes the slip path shorter and local strains less concentrated, rendering the impact-induced compressive stress layer more uniform and stable. Finally, a composite strengthened structure consisting of a fine-grained layer, a high dislocation density zone, and a residual compressive stress zone is developed in the surface layer. This coupled mechanism indicates that fatigue enhancement results from the synergistic evolution of microstructure and the residual stress field. Under the optimized condition, the residual compressive stress reached approximately −447 MPa and the fatigue life increased to $2.05 \times 10^5$ cycles, confirming the contribution of coordinated surface hardening and stress redistribution.

## 6. Fatigue Life Testing

### 6.1 Test Materials and Methods

Ti-6Al-4V titanium alloy was selected as the test material because of its extensive application in aerospace structures. Specimens with dimensions of 60 mm × 15 mm × 4 mm were prepared by grinding and polishing, and the initial surface roughness was controlled below $R_a = 0.8\mu m$. Abrasive water jet strengthening was performed using a CNC jetting platform. The jet pressure ranged from 180 to 260 MPa, the abrasive mesh number ranged from 80 to 140 mesh, the stand-off distance was maintained at 40 mm, and the impact angle was approximately 90°. Exposure time was varied from 30 to 90 s according to the selected processing condition. After treatment, surface morphology, XRD-based residual stress, and fatigue performance were evaluated. Fatigue tests were conducted using a high-frequency fatigue testing machine at a loading frequency of 20 Hz and a stress ratio of R=0.1. Three to five replicate specimens were tested for each processing condition to assess experimental reproducibility, and all tests were conducted under consistent environmental conditions.

### 6.2 Fatigue Life Test Results for Different Strengthening Processes

To evaluate the combined influence of jet pressure and exposure time on fatigue performance, several representative processing conditions were compared. Because the tested combinations do not constitute a complete factorial design, the results are interpreted as condition-dependent trends rather than fully independent pressure and time effects. A summary of the results is given in Table 1.

Table 1. Comparison of fatigue life under different spray pressures and exposure times

| Pressure (MPa) | Time (s) | Ra (μm) | Residual Stress (MPa) | Fatigue Life (cycles) |
|---|---|---|---|---|
| 180 | 30 | 0.92 | -320 | $1.28\times10^5$ |
| 180 | 60 | 1.05 | -358 | $1.46\times10^5$ |
| 220 | 30 | 1.08 | -402 | $1.73\times10^5$ |
| 220 | 60 | 1.16 | -445 | $1.98\times10^5$ |
| 260 | 30 | 1.24 | -468 | $1.84\times10^5$ |
| 260 | 90 | 1.39 | -512 | $1.76\times10^5$ |

As can be seen in Table 1, the fatigue life increased from 180 MPa to 220 MPa, from 1.28 × 10 MPa to 1.98 × 10 MPa, representing an increase of 54.7%. Meanwhile, the residual compressive stress was increased from -320 MPa to -445 MPa, suggesting that the strengthening effect was enhanced. However, at 260 MPa, the fatigue life was reduced to 1.76 × 10, which indicated that too high impact intensity led to an increase of 1.39 μm, thus weakening the fatigue property. In order to further analyse the influence of the grain size on the reinforcing effect, the experiment was carried out at constant pressure under different grain size conditions, and the results are summarized in Table 2.

Table 2. Comparison of fatigue life under different abrasive particle sizes

| Particle Size (mesh) | Pressure (MPa) | Ra (μm) | Residual Stress (MPa) | Fatigue Life (cycles) |
|---|---|---|---|---|
| 80 | 220 | 1.21 | -418 | $1.82\times10^5$ |
| 100 | 220 | 1.15 | -447 | $2.05\times10^5$ |
| 120 | 220 | 1.09 | -431 | $1.94\times10^5$ |
| 140 | 220 | 1.02 | -395 | $1.76\times10^5$ |

As shown in Table 2, increasing the abrasive size from 80 to 100 mesh increased fatigue life from $1.82 \times 10^5$ to $2.05 \times 10^5$ cycles, corresponding to a 12.6% improvement. At 100 mesh, the surface roughness was 1.15 μm and the residual compressive stress reached −447 MPa, indicating the best combined performance. Further increasing the abrasive size to 140 mesh reduced fatigue life to $1.76 \times 10^5$ cycles and residual compressive stress to −395 MPa. Therefore, the strengthening response exhibits a clear optimum rather than a monotonic dependence on abrasive size.

### 6.3 Model Validation and Error Analysis

To evaluate the internal consistency of the fatigue-life prediction model, experimental and predicted results were compared under six representative abrasive water jet processing conditions. The selected conditions cover jet pressures from 180 to 260 MPa and exposure times from 30 to 90 s, providing a quantitative basis for assessing prediction deviations across the investigated parameter range. The comparison focuses on the agreement between measured and predicted fatigue-life values, with relative error used as the principal evaluation indicator.

Table 3. Internal comparison of experimental and predicted fatigue life under different processing conditions

| Condition | Pressure (MPa) | Exposure Time (s) | Experimental Fatigue Life (cycles) | Predicted Fatigue Life (cycles) | Relative Error (%) |
|---|---|---|---|---|---|
| C1 | 180 | 30 | $1.28 \times 10^5$ | $1.22 \times 10^5$ | 4.69 |
| C2 | 180 | 60 | $1.46 \times 10^5$ | $1.39 \times 10^5$ | 4.79 |
| C3 | 220 | 30 | $1.73 \times 10^5$ | $1.68 \times 10^5$ | 2.89 |
| C4 | 220 | 60 | $1.98 \times 10^5$ | $2.05 \times 10^5$ | 3.54 |
| C5 | 260 | 30 | $1.84 \times 10^5$ | $1.91 \times 10^5$ | 3.80 |
| C6 | 260 | 90 | $1.76 \times 10^5$ | $1.69 \times 10^5$ | 3.98 |

Table 3 shows that the predicted fatigue-life values remain close to the experimental results under all six processing conditions. The minimum relative error is 2.89% for C3 at 220 MPa and 30 s, where the experimental and predicted values are $1.73 \times 10^5$ and $1.68 \times 10^5$ cycles, respectively. The maximum error is 4.79% for C2 at 180 MPa and 60 s. Under C4, the prediction differs from the experimental value by only 3.54%, despite the fatigue life reaching $1.98 \times 10^5$ cycles. At 260 MPa, errors remain below 4.0% for both C5 and C6. The overall error range of 2.89%–4.79% indicates stable agreement between measured and predicted values within the investigated dataset. However, because these conditions are not fully independent from model calibration, the comparison should be interpreted as internal verification rather than evidence of external generalization. To provide a direct evaluation of model accuracy, the experimental and predicted fatigue lives are compared in Figure 7. The two curves exhibit similar variation trends across all tested conditions, and no systematic overestimation or underestimation is observed.

The predicted results remain close to the experimental values, with errors ranging from 2.89% to 4.79%. The small deviation between the two curves confirms that the model captures the nonlinear relationship between process parameters, surface integrity, and fatigue life with acceptable accuracy. To further examine prediction consistency under different loading conditions, experimental and predicted fatigue-life values were compared at stress levels of 450, 500, and 550 MPa. Because only one representative experimental–prediction pair is available at each stress level, individual RMSE and MAPE values are not statistically appropriate. Therefore, relative error was

adopted to quantify the deviation between predicted and experimental fatigue life, as summarized in Table 4.

Table 4. Comparison of experimental and predicted fatigue life at different stress levels

| Stress Level (MPa) | Experimental Fatigue Life (cycles) | Predicted Fatigue Life (cycles) | Relative Error (%) | Stress Level (MPa) |
|---|---|---|---|---|
| 450 | $2.12 \times 10^5$ | $2.05 \times 10^5$ | 3.30 | 450 |
| 500 | $1.85 \times 10^5$ | $1.79 \times 10^5$ | 3.24 | 500 |
| 550 | $1.52 \times 10^5$ | $1.47 \times 10^5$ | 3.29 | 550 |

As shown in Table 4, fatigue life decreases from $2.12 \times 10^5$ to $1.52 \times 10^5$ cycles as the stress level increases from 450 to 550 MPa. The predicted values follow the same decreasing trend, ranging from $2.05 \times 10^5$ to $1.47 \times 10^5$ cycles. Relative errors are 3.30%, 3.24%, and 3.29% at 450, 500, and 550 MPa, respectively, indicating limited prediction deviation within the investigated stress range. Because only one representative value is available for each stress level, RMSE and MAPE are not reported separately. These results therefore demonstrate prediction consistency under the tested loading conditions rather than a statistically independent assessment of model robustness.

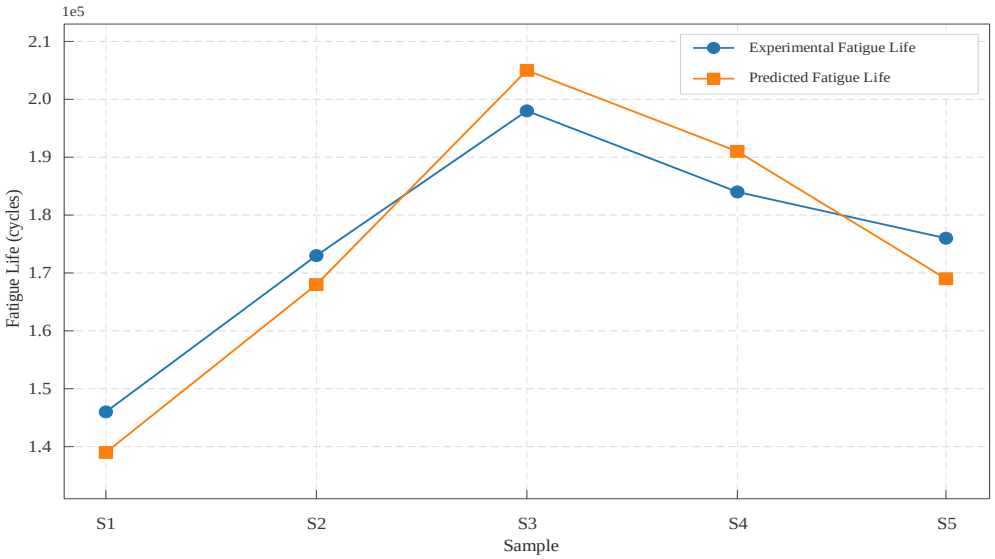



Fig. 7. Comparison between experimental and predicted fatigue life

### 6.4 Results Analysis and Discussion

The fatigue test results demonstrate that the strengthening response of Ti-6Al-4V is governed by the coupled effects of jet pressure, exposure time, abrasive particle size, residual compressive stress, and surface roughness. Increasing the jet pressure from 180 MPa to 220 MPa enhanced the residual compressive stress from approximately −320 MPa to −445 MPa and increased the fatigue life from $1.28 \times 10^5$ to $1.98 \times 10^5$ cycles. This improvement indicates that an appropriate increase in impact intensity promotes surface plastic deformation and the formation of a stable compressive stress layer. However, when the pressure reached 260 MPa and the exposure time was extended to 90 s, the surface roughness increased to 1.39 μm and the fatigue life decreased to $1.76 \times 10^5$ cycles, despite the higher compressive stress magnitude. The result confirms that excessive impact intensity can aggravate surface stress concentration and partially offset the beneficial effect of residual compression. Abrasive particle size also exhibited a distinct nonlinear influence on fatigue performance. At 220 MPa, the 100-mesh condition produced the highest fatigue life of $2.05 \times 10^5$ cycles, together with a residual compressive stress of −447 MPa and a surface roughness of 1.15 μm. Increasing the mesh number to 140 reduced the fatigue life to $1.76 \times 10^5$ cycles, indicating that insufficient particle impact energy weakens the formation of an effective strengthened layer. The prediction results remained consistent with the experimental observations, with errors mainly ranging from 2.8% to 4.8%. These results indicate that fatigue enhancement depends on an

appropriate balance among impact energy, residual stress development, and surface quality rather than on a monotonic increase in strengthening intensity.

## 7. Conclusions

The main conclusions are summarized as follows:

- Abrasive water jet surface hardening improves the fatigue resistance of aerospace-grade Ti-6Al-4V through the coordinated evolution of surface plastic deformation, grain refinement, surface hardening, and residual compressive stress. High-speed abrasive impact produces a plastically deformed near-surface layer and promotes microstructural refinement, while the resulting compressive stress field suppresses local tensile stress concentration under cyclic loading. The combined action delays fatigue crack initiation and reduces subsequent damage accumulation, confirming that fatigue enhancement originates from the coupling between microstructural reconstruction and mechanical-field evolution rather than from a single strengthening mechanism.
- The strengthening response shows a pronounced nonlinear dependence on process parameters. Increasing jet pressure from 180 MPa to 220 MPa increased fatigue life from $1.28 \times 10^5$ to $1.98 \times 10^5$ cycles, corresponding to an improvement of approximately 54.7%. Under the combined condition of 220 MPa and 100-mesh abrasive, the fatigue life reached the maximum value of $2.05 \times 10^5$ cycles, while the residual compressive stress reached approximately −447 MPa and the surface roughness remained at 1.15 μm. This parameter combination achieved the most favorable balance among impact energy, surface quality, and residual-stress development.
- Excessive strengthening intensity does not continuously improve fatigue performance. At 260 MPa with an exposure time of 90 s, the residual compressive stress increased to approximately −512 MPa, but surface roughness rose to 1.39 μm and fatigue life decreased to $1.76 \times 10^5$ cycles. The result reveals a competitive relationship between beneficial compressive-stress strengthening and detrimental roughness-induced stress concentration. Therefore, maximizing residual compressive stress alone cannot ensure optimum fatigue resistance; coordinated control of impact intensity and surface integrity is required.
- The process–surface integrity–fatigue performance framework provides a quantitative connection between strengthening parameters and fatigue behavior. Impact dynamics, surface roughness, grain characteristics, hardness, residual stress, and multi-source experimental information are integrated within a unified prediction procedure. Experimental and predicted fatigue-life values show consistent variation trends, with prediction errors maintained at approximately 2.8%–4.8% and an average error of about 3.8%. The limited error variation under different stress levels further indicates stable predictive performance within the investigated parameter range. This coupled framework provides a more systematic description of the transfer from process energy to surface integrity and subsequently to fatigue resistance.
- Limitations remain in the coverage of strengthening parameters and representative aerospace service conditions. Temperature variation, corrosive environments, variable-amplitude loading, complex component geometries, and long-term service interactions have not been comprehensively incorporated into the current validation framework. Future work should expand the experimental parameter domain, introduce multiscale surface characterization and high-fidelity Multiphysics simulation, and establish fatigue datasets under realistic service spectra. Further coupling of mechanism-based constraints with process optimization is expected to improve model transferability, identify robust strengthening windows, and provide more reliable guidance for fatigue-life extension and surface treatment design of critical aerospace-grade titanium alloy components.

## References

[1] Yao SL, Wang GY, Yu H, et al. Influence of submerged micro-abrasive waterjet peening on surface integrity and fatigue performance of TA19 titanium alloy. International Journal of Fatigue. 2022;164:107076. https://doi.org/10.1016/j.ijfatigue.2022.107076

[2] Wan L, Wang Y, Wang C, et al. Microstructure, tension-tension fatigue behavior, and enhancement mechanism of Ti6Al4V alloys peened by abrasive waterjet using solid waste sediment beads. Engineering Failure Analysis. 2025:110491. https://doi.org/10.1016/j.engfailanal.2025.110491
[3] Song F, Yao S, Liu L, et al. Submerged deflecting abrasive waterjet peening for improving the surface integrity and solid particle erosion resistance of Ti-6Al-4V alloy. Surface and Coatings Technology. 2023;470:129780. https://doi.org/10.1016/j.surfcoat.2023.129780
[4] Wan L, Cai J, Qian Y, et al. Surface integrity and fatigue performance of Ti6Al4V alloy peened by sinking bead abrasive jet. Journal of Materials Research and Technology. 2024;32:3169-3180. https://doi.org/10.1016/j.jmrt.2024.08.138
[5] Lv Z, Hou R, Wang R, et al. Investigation on surface integrity and fatigue performance in abrasive waterjet peening. Journal of the Brazilian Society of Mechanical Sciences and Engineering. 2022;44(11):520. https://doi.org/10.1007/s40430-022-03820-4
[6] Soori M, Arezoo B. Minimization of surface roughness and residual stress in abrasive water jet cutting of titanium alloy Ti6Al4V. Proceedings of the Institution of Mechanical Engineers, Part E: Journal of Process Mechanical Engineering. 2024;238(4):1613-1625. https://doi.org/10.1177/09544089231157972
[7] Wang Y, Wu M, Zhou S, et al. Study on the process of abrasive water jet peening for Ti6Al4V curved surfaces. Journal of the Brazilian Society of Mechanical Sciences and Engineering. 2025;47(7):315. https://doi.org/10.1007/s40430-025-05632-8
[8] Zhuang K, Li Y, Weng J, et al. Surface modification of titanium alloy using a novel elastic abrasive jet machining method. Surface and Coatings Technology. 2025;495:131573. https://doi.org/10.1016/j.surfcoat.2024.131573
[9] Zhang P, Gao Y, Jiang X, et al. Study on surface integrity and crack propagation mechanism of Ti/Al composite plates enhanced based on water jet peening. Vacuum. 2025;232:113818. https://doi.org/10.1016/j.vacuum.2024.113818
[10] Liu PHT. Review of Accomplishments in Abrasive-Waterjet Technology from Macro to Micro Machining: Part 2. In: Versatility of Waterjet Technology. Jenny Stanford Publishing; 2024:909-954. https://doi.org/10.1201/9781003510468-42
[11] Zhang P, Gao Y, Yue X, et al. Study on the fatigue performance and Residual Stress of subsurface fluid flow of 2519a aluminum alloy based on water jet peening. Vacuum. 2024;230:113648. https://doi.org/10.1016/j.vacuum.2024.113648
[12] Divyatheja K, Rajyalakshmi G. Optimizing water jet peening parameters for enhanced hardness and surface integrity of Ti6Al4V alloy: a multi-objective approach using Taguchi grey relational analysis. International Journal on Interactive Design and Manufacturing (IJIDeM). 2026;20(3):1335-1356. https://doi.org/10.1007/s12008-025-02468-3
[13] Chang S, Liu W, Tang J, et al. Cryogenic assisted abrasive waterjet machining of Ti-6Al-4V alloy: Thermo-mechanical optimization and AI-based surface integrity prediction. Sustainable Materials and Technologies. 2025:e01685. https://doi.org/10.1016/j.susmat.2025.e01685
[14] Lusi N, Catrawedarma I, Gebremariam M, et al. A four-decade of abrasive waterjet processing technology (1980-2023): a scientometric analysis. Manufacturing Review. 2025;12:15. https://doi.org/10.1051/mfreview/2025011
[15] Wang Y, Wu M, Miao X, et al. Optimization of abrasive water jet peening process for continuous curved surfaces of Ti6Al4V alloy. Journal of the Brazilian Society of Mechanical Sciences and Engineering. 2026;48(4):288. https://doi.org/10.1007/s40430-025-06233-1
[16] Li W, Wang S, Yang X, et al. Research progress on fatigue damage and surface strengthening technology of titanium alloys for aerospace applications. Metals. 2025;15(2):192. https://doi.org/10.3390/met15020192
[17] He K, Li KS, Chi YX, et al. Effect of abrasive waterjet peening on surface integrity and fretting fatigue life of a powder metallurgy superalloy. Tribology International. 2026:111937. https://doi.org/10.1016/j.triboint.2026.111937
[18] Yao SL, Zeng XT, Li KS, et al. Fretting fatigue life improvement of nickel-based superalloy GH4169 dovetail slots by deflecting abrasive waterjet peening process. International Journal of Fatigue. 2023;175:107832. https://doi.org/10.1016/j.ijfatigue.2023.107832
[19] Zhang P, Gao Y, Zhang J, et al. Inconel 718 alloy strengthening mechanism and fatigue life of microtexture-induced microjet coupled with cavifying water jet. Vacuum. 2024;222:113060. https://doi.org/10.1016/j.vacuum.2024.113060
[20] Liu PHT, Hovanski Y, Dahl ME, et al. Applications of abrasive-waterjets for machining fatigue-critical aerospace aluminum parts. In: Versatility of Waterjet Technology. Jenny Stanford Publishing; 2024:661-692. https://doi.org/10.1201/9781003510468-31
[21] Zhang P, Zhang J, Wang X, et al. Mechanistic Investigation into the Influence of Water Jet-Induced Surface Strengthening on the Tribological Performance of TC4 Alloy. Vacuum. 2026:115319. https://doi.org/10.1016/j.vacuum.2026.115319

[22] Wan L, Qian Y, Li Y, et al. Surface characteristics and tribological performance of Ti6Al4V peened by sinking bead abrasive waterjet. Journal of Manufacturing Processes. 2025;149:331-344. https://doi.org/10.1016/j.jmapro.2025.05.077
[23] Liu B, Zhang H, Wang X, et al. Research Progress on the Influence of Surface Treatment Techniques on Fatigue Properties of Titanium Alloys. Materials. 2026;19(8):1511. https://doi.org/10.3390/ma19081511
[24] Yue X, Zhang P, Gao Y, et al. Research progress, challenges, and prospects of high-pressure water jet surface modification technology for aerospace materials. Journal of Materials Durability and Engineering. 2025;1(1):4-22.
[25] Nagalingam AP, Gopasetty SK, Wang J, et al. Comparative fatigue analysis of wrought and laser powder bed fused Ti-6Al-4V for aerospace repairs: Academic and industrial insights. International Journal of Fatigue. 2023;176:107879. https://doi.org/10.1016/j.ijfatigue.2023.107879
[26] Lv Z, Hou R, Cui H, et al. Numerical study on fatigue crack behavior of 2024 Al alloy in abrasive waterjet peening. The International Journal of Advanced Manufacturing Technology. 2023;127(5):2979-2988. https://doi.org/10.1007/s00170-023-11742-1
[27] Kumar D, Gururaja S. Abrasive waterjet machining of Ti/CFRP/Ti laminate and multi-objective optimization of the process parameters using response surface methodology. Journal of Composite Materials. 2020;54(13):1741-1759. https://doi.org/10.1177/0021998319884611
[28] Xie J, Cao L, Qiao Y, et al. Post-Fatigue Residual Strength of Abrasiveless Waterjet-Treated Ti6Al4V as a Biomaterial: Xie, Cao, Qiao, Gao, Yang, Wang, Qi, Chen, Shemtov-yona, and Rittel. JOM. 2025;77(7):5374-5387. https://doi.org/10.1007/s11837-025-07331-0
[29] Siahpour P, Omar SMT, Griffin D, et al. Evaluating surface mechanical properties and wear resistance of Ti-6Al-4V alloy subjected to ultrasonic pulsed waterjet peening. Wear. 2024;550:205400. https://doi.org/10.1016/j.wear.2024.205400
[30] Abushanab WS, Moustafa EB, Harish M, et al. Experimental investigation on surface characteristics of Ti6Al4V alloy during abrasive water jet machining process. Alexandria Engineering Journal. 2022;61(10):7529-7539. https://doi.org/10.1016/j.aej.2022.01.004
[31] Siahpour P, Amegadzie MY, Moreau ED, et al. Surface characteristics and residual stress generation in Ti-6Al-4 V following ultrasonic pulsed water jet peening. Surface and Coatings Technology. 2022;445:128691. https://doi.org/10.1016/j.surfcoat.2022.128691
[32] Chakkravarthy V, Manojkumar P, Jerome S, et al. Effect of impact angle on hot corrosion resistance of abrasive water jet peened Ti-6Al-4V alloy. Surface and Coatings Technology. 2024;494:131523. https://doi.org/10.1016/j.surfcoat.2024.131523
[33] Ramakrishnan S, Singaravelu DL, Senthilkumar V, et al. Experimental investigation on microstructural characterization of machined Ti-6Al-4V using abrasive water jet machining. Sādhanā. 2022;47(2):83. https://doi.org/10.1007/s12046-022-01844-z
[34] Chang S, Liu W, Tang J, et al. Thermal effects and deformation mechanisms in abrasive waterjet machining: insights from Ti-6Al-4V alloy for broader applications. Journal of Materials Processing Technology. 2024;334:118643. https://doi.org/10.1016/j.jmatprotec.2024.118643
[35] Chang S, Liu W, Tang J, et al. Pressure-dependent thermal characteristics and microstructural evolution in abrasive waterjet-induced surface strengthening of Ti-6Al-4 V alloy. The International Journal of Advanced Manufacturing Technology. 2026:1-18. https://doi.org/10.1007/s00170-025-17360-3
[36] Rajesh M, Rajkumar K, Annamalai VE. Abrasive water jet machining on Ti metal-interleaved basalt-flax fiber laminate. Materials and Manufacturing Processes. 2021;36(3):329-340. https://doi.org/10.1080/10426914.2020.1832692
[37] Cano-Salinas L, Sourd X, Moussaoui K, et al. Effect of process parameters of Plain Water Jet on the cleaning quality, surface and material integrity of Inconel 718 milled by Abrasive Water Jet. Tribology International. 2023;178:108094. https://doi.org/10.1016/j.triboint.2022.108094
[38] Improvement of the Axial-Jet-Pump Performance using Modified Mixing Chamber Configuration and Inlet Swirling Flow.
[39] Optimal Performance of Water-Oil Axial Jet Pump in an Egyptian Offshore Oil Field.
[40] The Impact of Motive Nozzle Spacing and Surface Roughness on the Performance of Axial Water-Oil Jet Pumps in an Egyptian Offshore Oil Field: An Experimental and Computational Investigation.
[41] Computational and Experimental Study on the Effect of Motive Nozzle's Exit Length of Axial Water-Oil Jet Pumps in an Egyptian Offshore Oil Field.
[42] Computational and Experimental Study on the Water-Jet Pump Performance.